



# On the High-Temperature Oxidation Behavior of a Ta-Containing Quaternary Co-Base Model Alloy System with $\gamma/\gamma'$ -Microstructure - Influence of $\gamma'$ -Volume Fraction, Surface State, and Heating Condition on Alumina Growth

S. P. Hagen<sup>1</sup> · M. Weiser<sup>1</sup> · D. Kubacka<sup>2</sup> · E. Spiecker<sup>2</sup> · S. Virtanen<sup>1</sup>

Received: 17 July 2020 / Revised: 1 October 2020 / Accepted: 8 October 2020  
Published online: 27 October 2020  
© The Author(s) 2020

## Abstract

The improvement of the high-temperature oxidation resistance remains an ambitious goal for the design of new  $\gamma/\gamma'$ -strengthened Co-base superalloys, since their oxidation resistance beyond 800 °C still ranks behind their Ni-base counterparts. To better understand the origin of the poor oxidation resistance at higher temperatures, this study focuses on early stages of oxidation of four quaternary (Co-Al-W-Ta system) Co-base model alloys with a two-phase  $\gamma/\gamma'$ -microstructure and varying  $\gamma'$ -volume fraction at 800 °C, 850 °C and 900 °C. Based on time-resolved isothermal gravimetric analysis (TGA) in synthetic air and detailed electron microscopic analysis, the role of the  $\gamma$ -channel width (or  $\gamma'$ -volume fraction), the surface preparation prior to exposure (polishing versus shot-peening), and the heating conditions (synthetic air versus argon) on protective alumina growth is elucidated. Firstly, for alloys of increased  $\gamma'$ -volume fractions slower oxidation kinetics prevailed. Secondly, the two-phase microstructure was found to decisively affect the propagation of the internal oxidation front at the early stages of oxidation. Thirdly, shot-peening prior to exposure together with a lack of oxygen availability during heating was identified to foster protective alumina growth, accompanied by TCP-phase formation in the substrate. The critical role of a high Al availability in the alloy for a rapid growth of protective alumina and the relating challenges in alloy development regarding, for example, phase stability in this relatively novel Co-base alloy class are discussed in detail.

**Keywords** High-temperature oxidation · Cobalt base superalloys · Protective scales · TCP formation · Shot-peening · Oxygen partial pressure

---

✉ S. P. Hagen  
sebastian.p.hagen@fau.de

Extended author information available on the last page of the article

## Introduction

In 2006, Sato et al. [1] discovered an ordered  $\text{Co}_3(\text{Al},\text{W})$  phase ( $\gamma'$ ) with  $\text{L1}_2$  crystal structure in the ternary Co-Al-W-system. Coherent precipitates of this phase can form in the face-centered cubic (fcc) matrix ( $\gamma$ ) of Co-base alloys, resulting in a two-phase microstructure that is comparable to that of their Ni-base counterparts. The latter shows excellent creep properties and oxidation resistance, and are thus used in many high-temperature applications, such as gas turbines, where efficiency—according to the modified Brayton cycle—is strongly related to high combustion temperatures [2–4]. Since the opportunities for further optimisation of the well-established Ni-base superalloys are considered to be largely exhausted and an appropriate hardening mechanism for Co-alloys is now available, the fact of a 40 K higher melting point of pure Co compared to pure Ni generated major expectations toward the high-temperature properties of these materials [2, 5, 6]. According to compression creep testing the resistance against deformation at high temperatures of polycrystalline Co-base superalloys was recently shown to be very promising and even exceed that of the Ni-base alloys U720Li and Waspaloy at temperatures above 800 °C [7, 8]. However, their performance in harsh environments at temperatures beyond 800 °C still ranks behind their Ni-base counterparts [9, 10].

In the following, the prerequisites for the transition from internal to external growth of protective oxide scales that mainly base on Wagner's early considerations, are briefly recalled, and interconnected to further studies. Within literature, there is broad consensus that both the content of the respective solute species (e.g., Cr or Al) as well as their diffusivities are of crucial importance [11].

Regarding the *content* of elements forming protective scales (Cr or Al), a main obstacle in Co-based systems with  $\gamma/\gamma'$ -microstructure is the narrow phase field in which the hardening-phase is stable, and no TCP-phase formation is present. This issue is elucidated by Omori et al. for an isothermal section of the ternary Co-Al-W phase diagram at 900 °C [12]. To negotiate this hurdle, Ni is typically added in order to allow higher elemental contents of Al and Cr without losing the desired two-phase microstructure. For stabilizing the  $\gamma'$ -phase besides Ni-additions also Ta, Ti, and Hf additions are suitable [13–20]. The investigation of model systems granted systematic understanding of the effect of Ni and Cr on the oxidation mechanisms in Co-base alloys [21]. A major drawback regarding the oxidation resistance of Cr-containing Co-base alloys, however, is the unsatisfactory growth and sustainability of protective chromia scales. It was demonstrated that the oxidation resistance of Co/Ni-base two-phase model alloys with intermediate amounts of Al and Cr is mainly based on the formation of Cr-enriched oxide spinel barrier layers [21]. Particularly for alloys with a Co/Ni ratio > 1, massive nitridation (AlN) was evident [15]. To reach higher melting points and therefore increase the potential service temperatures, the Ni level in novel Co-base alloys should be kept low. Taking into account that Cr-rich oxidic barrier layers are temperature-limited in applications, it is well justified to investigate the mechanisms behind alumina formation in Ni-free Co-base alloys [22]. Promising results have

been gained recently by Stewart et al. describing a more complex Co-base system with up to six elements. Protective alumina formation at 1100 °C was achieved for an exposure duration of 1 h by a thorough optimization of the alloy. The identified composition containing a considerable amount of 36.5 at. % Ni elucidates the highly indispensable role of Ni, not only regarding phase stability, but also oxidation resistance for Co-base alloys [17].

Besides the content, also the *diffusivity* of the scale forming elements plays an important role in Wagner's criterion for protective scale growth [11]. Therefore *firstly*, the alloy composition itself affects the transport velocity of all elements. The lower diffusivity of relevant solute atoms in Co in comparison with Ni is a strong indication that diffusion-controlled processes in general may be slower in Co- than in Ni-base superalloys [5]. Previous studies demonstrated a significant impact of the W-content in ternary Co-base alloys, with nominal similar Co- and Al-levels, on the formation of lateral alumina scale sections [23, 24]. Therefore, a decelerating influence of higher concentrations of heavy elements such as Ta and W on diffusion-driven processes can be assumed [25–28]. Additionally, the role of the two-phase microstructure on elemental transport, especially during the early stages of oxidation, can be seen as a crucial. Weiser et al. demonstrated for a ternary Co-base alloy with  $\gamma/\gamma'$ -microstructure the exclusive formation of discrete alumina particles in the  $\gamma$ -channels at the internal oxidation front (IOF). These oxide particles were identified to grow due to the preferential Al delivery from the surrounding  $\gamma$ -phase during the first hours of exposure to air. After these early stages of scale growth, Al depletion additionally affects the adjacent  $\gamma'$ -precipitates [29]. Due to this time dependency of the spatial expansion of the depletion-affected zone, it is not out of the question if the microstructure by itself could affect the progress of the IOF and by that affect the protective scale growth of a two-phase alloy.

Since subsurface crystal defects such as grain boundaries or dislocations are known to act as short-circuit paths for diffusion, the elemental fluxes of the solute protective scale forming elements (Cr and Al) *secondly*, strongly depend on the pre-history of the material. Plastic deformation applied for example via shot-peening (SP) increases the dislocation density within a certain depth in proximity to the surface. This technique is often used for improving mechanical properties, since the higher dislocation density leads to an increased surface hardness and compressive stresses. At high temperatures these dislocations can act as short-circuit paths for diffusion as described by Grabke et al. for Cr-containing steels [30]. The study demonstrated the formation of additional grain boundaries at sufficient exposure temperatures due to recrystallization. Since the dislocations are not fully annihilated by recrystallization, finally both new grain boundaries and residual dislocations can be seen as causative for fostered protective oxide growth [30]. Leistikow et al. demonstrated that the degree of cold work and also the grain size strictly correlate to the corrosion resistance of austenitic Alloy 800 (Fe–Ni–Cr) during steam oxidation at 600 °C due to an enhanced chromia formation [31]. Wang reported a strong improvement of the oxidation resistance at 1000 °C for K38G (Ni-base superalloy) comparing nanocrystalline with casted large-grained samples due to the enforced growth of protective alumina [32]. For Co-base superalloys, (Co–Al–W–B system) Klein et al. described a positive effect of grain boundaries on internal alumina

formation at 800 °C and 900 °C by comparing single-crystalline alloy with a polycrystalline alloy of the same nominal composition that was, however, reversed at higher temperatures (1000 °C). Consequently, it can be assumed that surface preparation of Co-base alloys might also have a considerable effect on the transport of protective scale forming elements.

The present study elucidates the short-term oxidation mechanisms of a series of quaternary Co-base model alloys (Co-Al-W-Ta system) with two-phase  $\gamma/\gamma'$ -microstructure at 800 °C, 850 °C and 900 °C in synthetic air with regard to alumina formation. Results of time-resolved isothermal gravimetric analysis (TGA) and scanning electron microscopy (SEM) investigations are complemented by electron backscatter diffraction (EBSD), electron probe micro analysis (EPMA), and scanning transmission electron microscopy (STEM) investigations.

The influence of a varying  $\gamma'$ -volume fraction (i.e., the  $\gamma$ -channel width) on the progress of the IOF is elucidated for polished (Pol) samples within the first part of this manuscript. In the second part, possible strategies to initiate the growth of diffusion limiting alumina sections at the IOF are explored. The susceptibility of the investigated alloys to accelerated alumina formation due to plastic deformation in the subsurface region (shot-peening (SP) prior to exposure) and due to heating conditions (influence of oxygen partial pressure) is assessed.

## Experimental Procedures

### Sample Materials

The Co-base superalloy system that is investigated in this work is designed to vary the volume fraction of the  $\gamma'$ -phase without varying the composition of the individual phases,  $\gamma$  and  $\gamma'$  [33]. This peculiarity is supposed to be obtained by conducting compositional changes along a schematic tie-line in a Co-(Al,W,Ta) quasi-binary system [33]. According to [33], the four alloys in this work are based on exhibited nominal volume fractions of 20%  $\gamma'$  (referred to as VF20 in the following), 40%  $\gamma'$  (VF40), 50%  $\gamma'$  (VF50) up to 60%  $\gamma'$  (VF60) after heat-treatment. These nominally designated values that are predicted due to compositional changes along the tie-line, were compared to calculated volume fractions by Bezold et al.. For the latter area fractions achieved via classical metallurgical cross-sectioning were transferred to volume fractions anticipating cubic morphology as well as equal size and distribution of the hardening-phase [33]. The comparison revealed a discrepancy between both values [33]. It was decided to keep the nominal volume fractions to name the alloys for this manuscript, since such values are suitable to qualitatively describe the microstructure as can be seen in Fig. 1. VF40 and VF50 were cast as single crystals with an intended  $\langle 001 \rangle$  orientation along the rod-axis via Bridgeman investment casting by the Institute of Metals Science and Technology (WTM, University of Erlangen-Nürnberg (FAU), Germany). Samples of VF20 and VF60 are in polycrystalline state. The nominal compositions of the alloys are given in Table 1. The actual overall compositions were determined by EDX (FE-SEM, Hitachi S-4800) and are given in

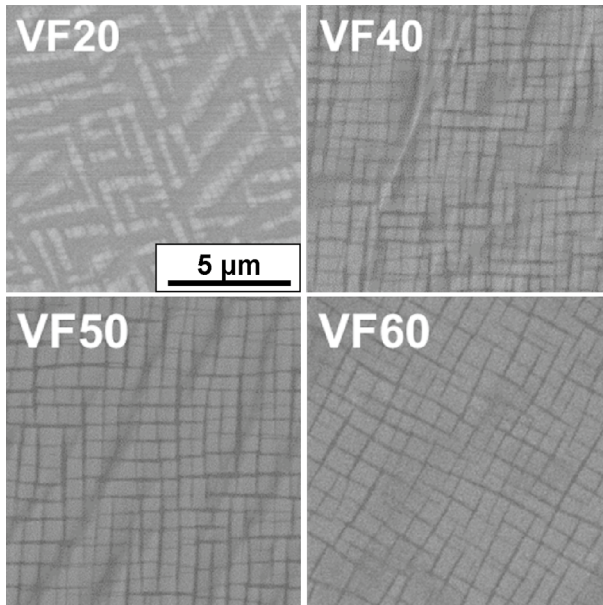


**Fig. 1** BSE-micrographs of investigated model alloys after heat-treatment

**Table 1** Nominal elemental compositions of the alloys VF20–60 in at. % [33]

Alloys	Co	Al	W	Ta
VF20	84.4	8.8	5.7	1.1
VF40	82.1	8.9	7.3	1.7
VF50	81.1	8.9	8.0	2.0
VF60	79.8	8.9	9.0	2.3

**Table 2** Actual elemental composition of the alloys measured by SEM–EDX in at. %

Alloys	Co	Al	W	Ta
VF20	83.7	9.8	5.7	0.7
VF40	80.6	9.5	7.4	2.5
VF50	78.4	9.8	9.1	2.8
VF60	79.5	7.8	9.7	3.0

**Table 2.** To gain equal elemental distribution within the crystal, a heat-treatment comprising a homogenization annealing step for 24 h at 1350 °C was conducted, prior to an aging-heat treatment (100 h at 900 °C) for initiating the targeted  $\gamma/\gamma'$ -microstructure. Figure 1 reveals the resulting  $\gamma/\gamma'$ -microstructure of the alloys and demonstrates that no further phases were formed. Due to the preferential partitioning of W and Ta into the  $\gamma'$ -phase, the cuboidal precipitates appear brighter than the surrounding matrix-phase ( $\gamma$ ).

## Surface Modifications

Samples with a thickness of 1 mm were cut from the rods after heat treatment. After manual grinding up to a grit size of 1200 SiC and subsequent polishing with a 9  $\mu\text{m}$  diamond suspension, sample preparation was varied to achieve different surface conditions. Either shot-peening (samples referred to as “SP” in the following) or polishing down to 1  $\mu\text{m}$  grit size (referred to as “Pol” in the following) was chosen as final step during sample preparation. For SP a glass shot (MS400BT from IEPCO, Switzerland) with a nominal shot-diameter in the range of 40–70  $\mu\text{m}$  was used with a pressure of about 2 bar. The samples were manually shot-peened from both sides for a time of 1 min each, from a distance of approximately 2 cm and an impact angle of 90°. To elucidate the influence of surface roughness and possible surface contamination by indentation of residual glass particles, a sample of VF40 was carefully polished to 1  $\mu\text{m}$  surface finish after SP. Therefore, a pressure of 5 bar and a mask was used. The mask guarantees a sharp transition from neighboring districts being shot-peened and untreated on the same sample.

## Oxidation (Isothermal Thermogravimetric Analysis)

The time-resolved isothermal oxidation experiments were performed at 800 °C, 850 °C, and 900 °C for different exposure times in a SETSYS Evolution 1650 TGA from SETARAM. The exposure was conducted in synthetic air, whereas the atmosphere during heating was either synthetic air (referred to as “Air, air samples or air experiments” in the following) or argon (referred to as “Argon, Argon-samples or Argon-experiments” in the following). Heating and cooling were performed with a rate of 25 K/min. Gas flow rates were set to 20 ml/min, which equals a laminar gas velocity of about 7.86 cm/min. For air experiments, the taring of the scale was conducted prior to heating, and the heating time is not included in the nominal exposure time of an experiment. Mass changes during heating were recorded and considered for the plotted mass-gain diagrams.

To guarantee a sudden and well-defined change of the atmosphere, a different approaches were used for the argon experiments. For the latter, heating was conducted in argon atmosphere followed by an evacuation step of 20 min duration. Subsequently, the interior of the furnace was filled with synthetic air. Since the mass-signal is highly affected by changing hydrostatic uplift forces derived by the increasing total pressure during this refilling-step, taring was conducted 10 min after the initiation of gas flow. Thus, all argon mass-gain curves in this work do not consider possible mass changes that might have occurred during heating (35 min to 900 °C) and during the subsequent 30 min (20 min evacuation 10 min refilling) period. To allow a conservative (Argon is expected to increase alumina formation) comparison to the air experiments, the respective curves were modified. Firstly, the specific mass-gain values after 10 min oxidation at 900 °C of the respective air-samples were added as a fixed value to the continuous specific mass-gain data obtained for the argon experiments. Secondly, the time values were corrected by adding 45 min that

represents the duration of heating to 900 °C (35 min) and the subsequent refilling step (10 min). The 20 min step of evacuation is not included, since the anyway low oxygen partial pressure in argon atmosphere further decreases during evacuation.

## Preparation of Cross-Sections and Microscopic Characterization

Ni-plating was conducted prior to metallurgical preparation of cross-sections. Firstly, a thin Au-layer was applied by sputtering. Subsequently, galvanostatic electroplating was performed with a  $\text{NiSO}_4$ -based solution at a current density of  $15 \text{ mA/cm}^2$  for 30 min. Subsequently, samples were cut in half by a water-cooled low-speed saw. For the cross-section preparation an ion-milling system (IM4000 from Hitachi) was used. For scanning electron microscopy (SEM) investigations, a LYRA3 SEM from Tescan was used. Elemental maps and line-scans were determined by electron probe microanalysis (EPMA, JXA-8100 from JEOL) to elucidate the elemental distribution across the oxide scale and adjacent depletion-affected regions. The TEM lamella was prepared exemplarily from VF-40 sample, using dual-beam SEM–FIB Helios NanoLab 660. Scanning transmission electron microscopy (STEM) in HAADF mode together with energy dispersive X-Ray spectroscopy was used for chemical analysis of the lamella. A double-corrected FEI Titan Themis TEM equipped with SuperX detector was operated at 300 kV.

## Results and Discussion

### Oxidation Kinetics of Polished Samples

Figure 2 provides the TGA results for polished samples at 800 °C, 850 °C and 900 °C after heating in air.

In addition to the general trend of strongly increasing mass-gain for higher temperatures, alloys with higher volume fractions of  $\gamma'$  evidently developed slower oxidation kinetics at all temperatures. Since the Al-content is highly comparable for

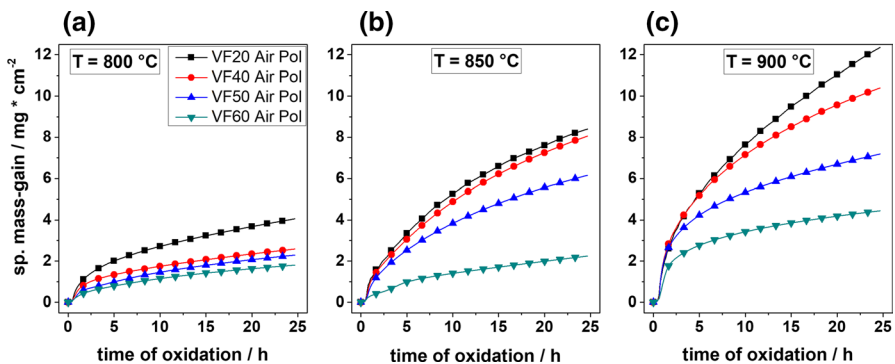


**Fig. 2** Continuous specific mass-gain (mass-gain per surface area) for polished (Pol) samples oxidized for 24 h at **a** 800 °C, **b** 850 °C and **c** 900 °C. All curves for samples heated in synthetic air (Air)

VF20 (9.8 at.%), VF40 (9.5 at.%), and VF50 (9.8 at.%) and even lower for VF60 (7.8 at.%) according to Table 2, this is not expected to be the decisive reason for the pronounced dependency of the  $\gamma'$ -volume fraction in the order of oxidation resistance. Instead, the W- and Ta-content and by that the channel width (width of  $\gamma$ -phase separating two neighboring precipitates) are varied to a significantly larger extent than the Al-content.

In order to further discuss the oxidation behavior of the VF alloys, cross-sections after 24 h of exposure are elucidated in the following (BSE-micrographs in Fig. 3). Since VF20 suffered from severe spallation during cooling, Fig. 3 is limited to VF40, VF50, and VF60. Each scale is composed of an outer Co-rich oxide layer (exemplarily marked as “Co-Ox.” in Fig. 3a), possessing a significant amount of porosity that is especially pronounced after exposure at 850 °C and 900 °C. Underneath this outer oxide scale a deeply penetrating internal oxidation zone (IOZ) can be found that also includes a considerable degree of pores. Within the IOZ lateral cracks can be seen. The severity of the latter clearly diminished with the number of conducted milling steps for preparation of the cross-sections (thus with increasing distance from the original cut). Therefore, it can be expected that wide cracks develop during the mechanical cutting due to the evidently high porosity in this scale region. Overall, the scale thicknesses are in agreement with the mass-gain results.

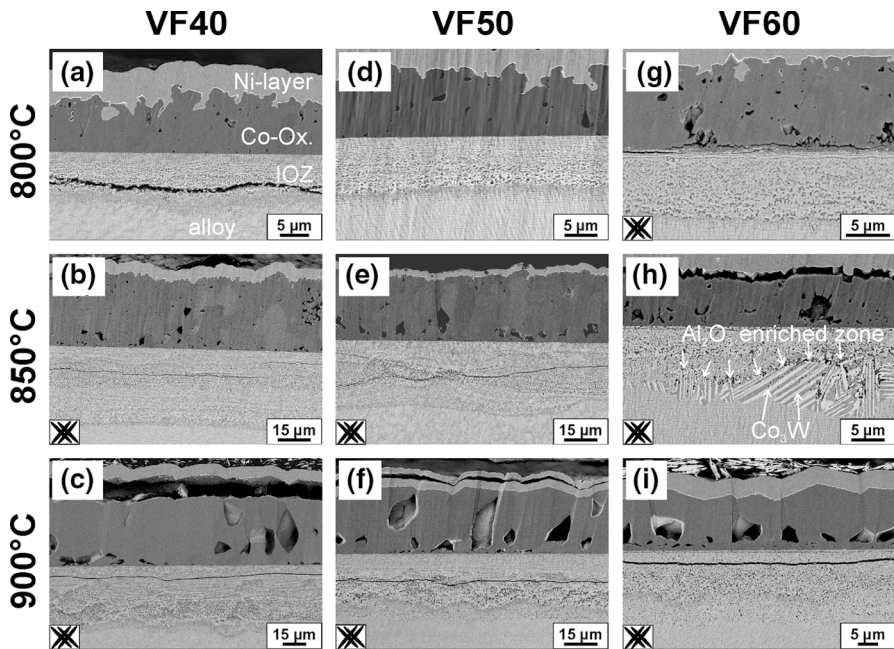


**Fig. 3** BSE-micrographs of cross-sections of VF40 (left column: **a**, **b** and **c**), VF50 (middle column: **d**, **e**, and **f**) and VF60 (right column: **g**, **h** and **i**) after 24 h of exposure at 800 °C (upper row: **a**, **d** and **g**), 850 °C (middle row: **b**, **e**, and **h**) and 900 °C (bottom row: **c**, **f** and **i**). If  $\text{Co}_3\text{W}$ -phase is present it is highlighted with the use of a pictogram. All micrographs reveal to the TGA samples shown in Fig. 2 (polished and heated in synthetic air)



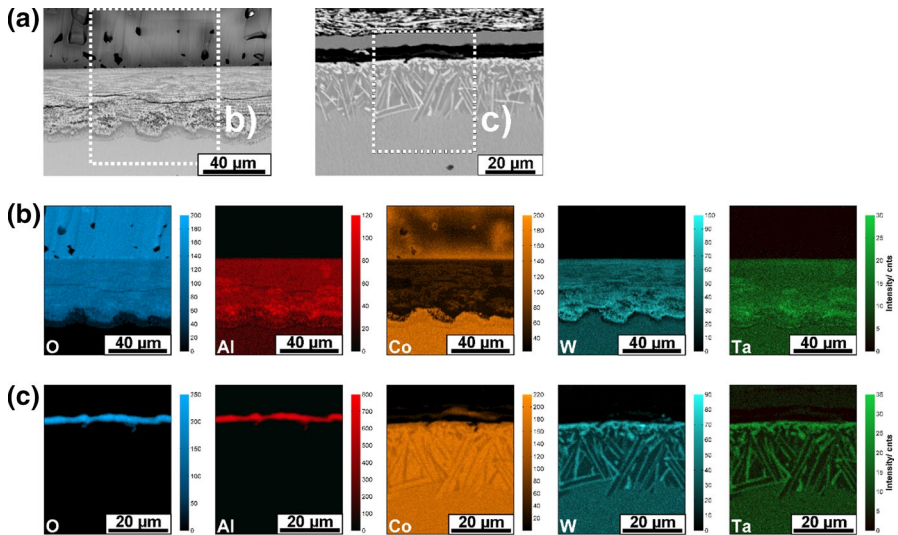


**Fig. 4** BSE-micrographs of oxide scales (VF40, heated in Argon and exposed for 36 h at 900 °C) and corresponding elemental distribution maps determined by EPMA (regions are marked by white rectangles). **a** left and **b**: Pol. **a** right and **c**: SP

The EPMA maps in Fig. 4a elucidate the elemental distribution for a polished VF40 sample that has been oxidized for 36 h at 900 °C (in Fig. 4b; for sake of clarity also the EPMA maps for shot-peened oxidized sample are shown – this will be discussed later in the manuscript). Since the overall appearances of the oxide scales are similar according to Fig. 3, it is assumed that the results can be seen qualitatively valid also for VF20, VF50 and VF60. The maps indicate that the outer oxide scale mainly consists of Co and oxygen. Furthermore, pronounced depletion of Co is present within the IOZ, whereas all further alloying elements show less long-range deviations from their base alloy content. Within the porous IOZ Al, Ta and W oxides are formed. Alumina is the oxide with the lowest average atomic mass and consequently, Al-enriched areas in the EPMA map match with the dark regions in the BSE-micrographs in Fig. 4. However, there are no continuous alumina layers. Instead magnified micrographs of respective areas show an increased density of separated single alumina precipitates (e.g. Figures 3h, 5 and 6i). At the transition zone between IOZ and alloy it is noteworthy that the Al-content decreased abruptly, leading to a thin Al depleted zone of approximately 1.5 μm thickness that encases the IOF. A similar behavior is found for W but less for Ta. In contrast to those latter elements the oxygen-content decreases steadily toward the alloy.

To further clarify the elemental distribution at the IOF and to confirm whether alumina forms also in quaternary Co-base alloys as distinct oxide particles that mainly grow due to the Al-supply by the  $\gamma$ -phase as described for a ternary system [29], STEM-EDX results are presented for the intermediate exposure temperature (850 °C) in Fig. 5. From the elemental distribution maps in Fig. 5a it can be concluded that high Al accumulation is present within the dark oxide particles that are

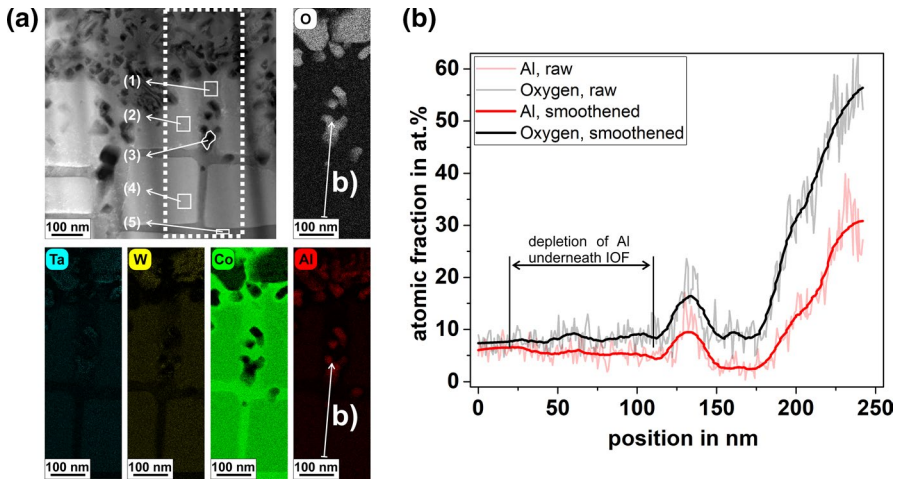


**Fig. 5** Elemental distribution at the IOF/alloy interface of VF40 (PoI) exposed for 30 min at 850 °C in synthetic air. Figure **a** depicts a HAADF-STEM-micrograph where the position of the elemental maps is marked by the large rectangle (dashed white line). The compositions of the numbered regions are provided in Table 3. Figure **b** shows the elemental concentration of Al and oxygen along the line-scan of which the position is given by the arrows in **a**, with 0 nm corresponding to the crossline of the arrow

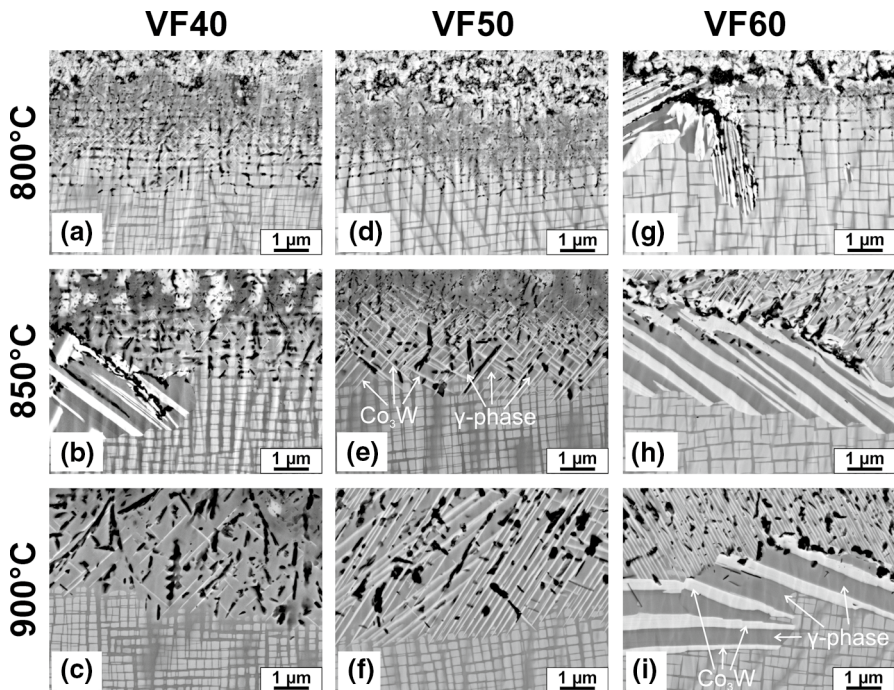


**Fig. 6** BSE-micrographs of IOZ/alloy interface of VF40 (left column: **a**, **b** and **c**), VF50 (middle column: **d**, **e**, and **f**) and VF60 (right column: **g**, **h** and **i**) after 24 h of exposure at 800 °C (upper row: **a**, **d** and **g**), 850 °C (middle row: **b**, **e**, and **h**) and 900 °C (bottom row: **c**, **f** and **i**). Exemplarily  $\text{Co}_3\text{W}$  and residual  $\gamma$ -phase is highlighted in **e** and **i**

**Table 3** STEM-EDX measurement of the elemental concentration within the highlighted (numbered) areas in Fig. 5 a) in at. %

Position	Description	O	Al	Co	Ta	W
(1)	$\gamma$ - close to IOF	8.11	0.87	83.21	2.84	4.96
(2)	$\gamma'$ - close to IOF	5.46	5.40	74.63	6.12	8.39
(3)	$\text{Al}_2\text{O}_3$	64.33	31.78	1.9	2.35	0.05
(4)	$\gamma'$	5.26	6.17	73.49	6.32	8.76
(5)	$\gamma$	7.98	5.92	82.59	1.49	2.02

visible in the HAADF-STEM-micrograph. A quantification from the highlighted area (position (3)) of Fig. 5a, given in Table 3, indicates the formation of  $\text{Al}_2\text{O}_3$  as distinct particles. Furthermore, the Al-level within the  $\gamma$ -phase close to the IOF reveals a difference of approximately 5 at. % compared to the one of the unaffected matrix below the interface (position (5)). This finding quantitatively indicates the role of the  $\gamma$  channel regarding Al transport toward the IOF. The continuous line-scan in Fig. 5b clearly demonstrates a steady depletion of Al along the  $\gamma$  channel and substantiates this finding. In contrast, the comparison of position (2) (5.4 at. % Al) and (4) (6.17 at. % Al) in Fig. 5a indicates that Al-contents in  $\gamma'$  only marginally decrease with increasing distance from the IOF. Consequently, the hardening-phase acts as the main reservoir for Al in the internal oxidation zone at this stage of reaction. This is especially noteworthy considering the severe depletion of the  $\gamma$ -phase in direct proximity to position (2). Besides accelerated Al transport, also preferential diffusion of oxygen in the  $\gamma$ -phase can be ascribed according to Fig. 5a and Table 3. Positions (4) and (5) indicate that the oxygen-content in the  $\gamma$ -phase is higher than within the precipitate, even though the EDX measurement in the  $\gamma'$ -phase (position (4)) originates from a region closer to the IOF. The fact that the progress of internal oxidation is sustained by the transport of oxygen and not even diminutive oxide precipitates can be found within the hardening-phase, further substantiates the assumption of a faster oxygen transport within the channels. These STEM-EDX results on elemental transport are expected to be qualitatively also valid for VF20, VF50, and VF60 as well as for 800 °C and 900 °C, since the appearance of the IOF is qualitatively highly comparable.

After 24 h of exposure, however, a new phase that shows a rod-like shape with a high aspect ratio appearing bright in the BSE-micrographs formed. This phase cannot only be seen in Fig. 3h but also at the transition zones IOZ/alloy (Fig. 6) of all further cross-Sects. (24 h), except for VF40 (Fig. 6a) and VF50 (Fig. 6d) after oxidation at 800 °C. Due to its small size, the EPMA map in Fig. 4a does not resolve this phase even though it is present. According to literature, the phase can be identified as  $\text{Co}_3\text{W}$  and is formed due to Al depletion caused by alumina formation within the IOZ [34]. Figure 6 indicates that the  $\text{Co}_3\text{W}$ -phase often exhibits a bimodal size distribution. Whereas the small rods are formed homogeneously along the entire IOF, the occurrence of the large precipitates (s. Figure 6b, g, h, i) strongly depends on the accumulation of alumina precipitates in direct proximity above (s. also dark alumina enriched zone above the TCP-phases in Fig. 3h). This locally accumulated alumina formation might be affected by stochastic factors. The ion-milling based

cross-sections are solely representing a confined part of a sample, therefore locally observed severity of the TCP-phase occurrence should be interpreted with reservation as a valid measure of depletion.

Since TCP-phase formation is known as a consequence of Al depletion, it can be assumed that also increasing exposure times foster  $\text{Co}_3\text{W}$  growth. Coarser alumina particles form at longer exposure times at the IOF and consequently lead to more extensive Al depletion in the surrounding alloy. Thus, additional samples of VF20, VF40, VF50 and VF60 were oxidized for 12 h, s. Figure 7 (instead of 24 h, Fig. 6). When comparing these cross-sections with those of samples after 24 h exposure (Fig. 6), it is obvious that by shortening the exposure time, the inset of TCP-phase formation is less probable to be reached. The tendency of enhanced growth of TCP-phases during longer exposure times was furthermore verified after 500 h oxidation of VF50 at 900 °C s. Figure 8. The displayed cross-section exhibit massive TCP formation below the IOF. Additionally, high volume fractions of  $\gamma'$  (i.e., high W- and Ta- contents) and high exposure temperatures promote TCP-phase formation according to both Figs. 6 and 7. When TCP-phases form, or in other words, sufficient Al depletion is reached, two cases must be distinguished. Case (I), as e.g., depicted in Fig. 6e, indicates an IOF showing TCP-rods that are embedded into the  $\gamma$ -phase and

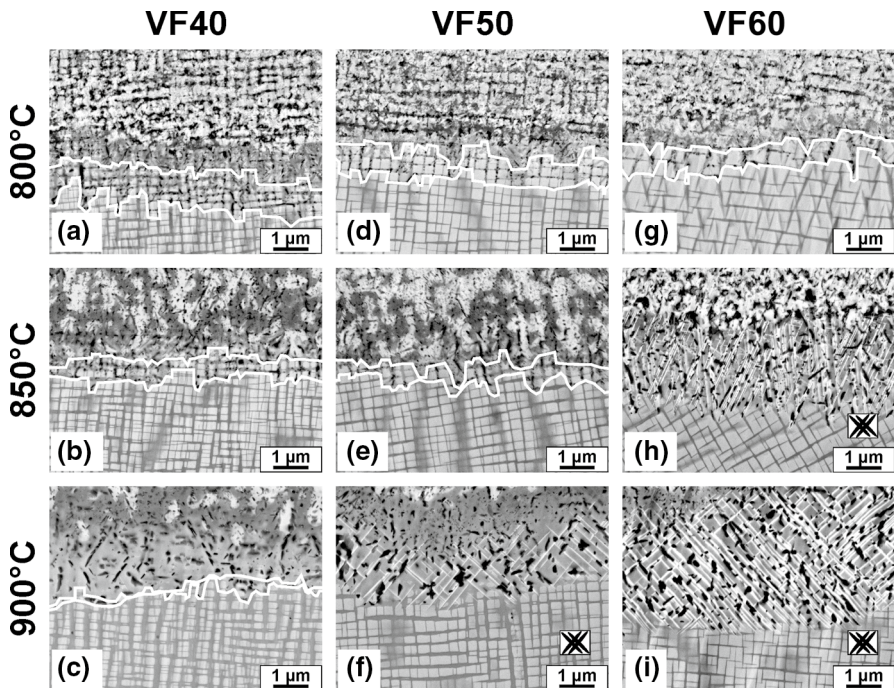


**Fig. 7** BSE-micrographs of IOZ/alloy interface of VF40 (left column: **a**, **b** and **c**), VF50 (middle column: **d**, **e**, and **f**) and VF60 (right column: **g**, **h** and **i**) after 12 h of exposure at 800 °C (upper row: **a**, **d** and **g**), 850 °C (middle row: **b**, **e**, and **h**) and 900 °C (bottom row: **c**, **f** and **i**). Occurrence of  $\text{Co}_3\text{W}$ -phase is highlighted with the use of a pictogram, s. Figure 3

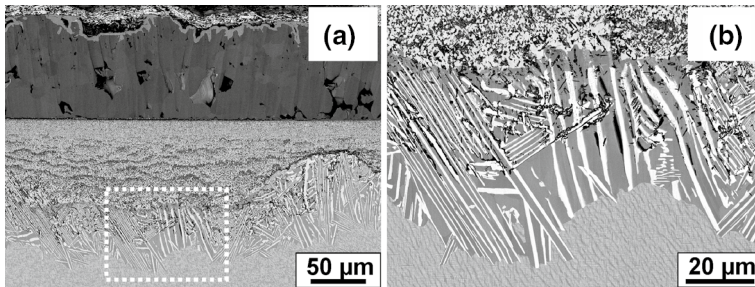


**Fig. 8** BSE-micrographs of a cross-section of VF50 (pol) after 500 h exposure at 900 °C in synthetic air. **a** shows the total scale system, **b** the marked area of figure a in higher magnification

alumina precipitates, whereas the  $\gamma'$ -phase is almost fully dissolved. Case (II), as e.g., depicted in Fig. 6i), indicates an IOF that shows case (I)-composition but with an additional layer of TCP- and  $\gamma$ -phase underneath. The latter layer is also prone to  $\gamma'$ -depletion. Case (II) is associated with local enrichment of alumina and thus a more pronounced depletion. Furthermore, after a duration of 12 h exposure the role of the channel width and the two-phase microstructure on the morphology of the IOZ/alloy interface and the distribution of the alumina particles within this zone can be elucidated in more detail since less TCP-phases are present. It can be confirmed that alumina formation primarily proceeds within the  $\gamma$ -channels that are surrounded by unaltered  $\gamma'$ -precipitates during early stages of oxidation. This has been noticed for VF40 and VF50 after 24 h at 800 °C and prevails for 12 h oxidation experiments for VF40, VF50 and VF60 samples at 800 °C, VF40 and VF50 samples at 850 °C and VF40 samples at 900 °C (s. Figure 7). In the investigated Co-base alloys, alumina exhibits insufficient lateral growth which is needed to form a diffusion limiting oxide layer. According to Zhao et al. the simultaneous formation of numerous discrete oxide precipitates can be attributed to pronounced rates of alumina nucleation [35]. The  $\gamma'$ -precipitates are subjected to a slower oxidation-related attack that is accompanied by an evident shape loss as it is depicted for the STEM-results (for 30 min exposure at 850 °C). Due to that, a transition zone can be defined in which the hardening phase is partially attacked but still present, whereas the matrix-phase is strongly affected by oxidation. This transition region is marked by the white lines in Fig. 7. The fact that  $\gamma$  is preferentially attacked was already demonstrated for ternary Co-Al-W systems [29]. The main reason for this characteristic morphology of the IOF during the first hours of oxidation is presumably that the oxygen transport almost exclusively proceeds in the  $\gamma$ -phase as indicated by the STEM-EDX results provided in Fig. 5a and Table 3. The influence of the channel width on the thickness of this transition zone can therefore be quantitatively evaluated and shows a direct correlation between the microstructure and the oxidation mechanisms at the oxide/alloy interface

Following the assumption that the different transport properties for oxygen between the two phases play the key role during the formation of this zone, the thickness of this region ( $d_{trans}$ ) can be approximated as the average distance between the white lines (s. Figure 7) measured along the  $\gamma$ -channels and not rectangular to

**Fig. 9** Average distance  $d_{Trans}$  after 12 h of oxidation at 800 °C, 850 °C and 900 °C for micrographs of Fig. 7 (VF40, VF50 and VF60). For the measurements each channel was considered thus the measured values differ in number (least 18, at most 38). Error bars show the standard deviation. All samples were heated in synthetic air

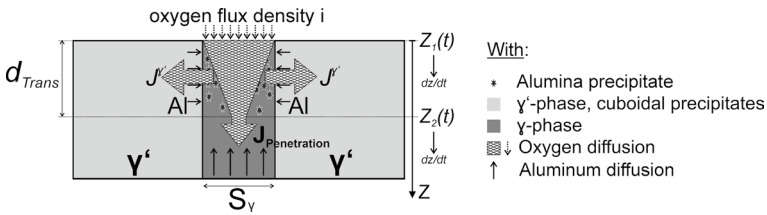
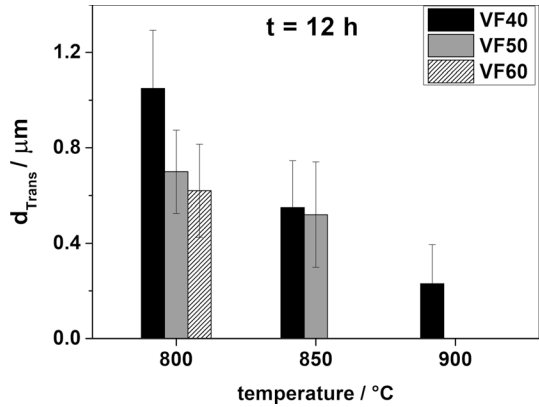


**Fig. 10** Scheme of proposed diffusional fluxes within the IOZ/alloy interface. Outer oxide scale and IOZ are not shown

the surface. Figure 9 illustrates the dependency of the  $\gamma'$ -content and exposure temperature on  $d_{trans}$ .

At 800 °C, a distinct correlation between volume fraction and thickness of the transition zone can be identified. Samples show wider  $d_{trans}$  for lower  $\gamma'$ -contents. For specimens after oxidation at 850 °C, the identical trend appears, however, less pronounced. The comparison of  $d_{trans}$  of VF40 at different temperatures indicates a decrease in thicknesses with increasing exposure temperatures. Since TCP-phase formation is evident for VF60 at 850 °C and for VF50 and VF60 at 900 °C (s. Figure 7f, h and i), the measurements of  $d_{trans}$  (Fig. 9) could not be conducted for experiments of the respective alloys at these temperatures. Via a simplifying schematic drawing (Fig. 10), a qualitative explanation is proposed in the following to explain the dependency between  $d_{trans}$  and the volume fraction of  $\gamma'$ . The scheme represents a vertical  $\gamma$ -channel and two neighboring  $\gamma'$ -precipitates that are allocated at the oxide/alloy interface. Due to simplification, horizontally aligned  $\gamma$ -channels are not considered.  $Z_1$  is the borderline within the IOZ above which the  $\gamma'$ -precipitates are fully oxidized and is consequently representing the upper white line in Fig. 7 ( $Z_2$  represents the lower white line).

Based on the oxygen distribution, elucidated by the STEM-EDX investigations, it is assumed that the oxygen flux density  $i$  in  $\gamma$  exceeds the flux density in  $\gamma'$  at this interfacial region (Fig. 10). The resulting oxygen flux entering the channel is described by  $J_{Penetration}$ . The latter leads to a steadily proceeding increase in the

oxygen activity within the channel, until the driving force is sufficient for the formation of alumina. This is the case for  $Z_1 < Z < Z_2$  according to Fig. 10. The first alumina precipitates, symbolized by black stars in Fig. 10, nucleate and coarsen due to the Al-supply of the adjacent  $\gamma$ -phase (indicated by the vertical solid-line arrows in Fig. 10). With increasing Al depletion of the  $\gamma$ -phase, the  $\gamma'$ -precipitates progressively act as Al-reservoirs, leading to the inset of an additional Al-supply (horizontal solid-line arrows in Fig. 10). The oxygen that is consumed by the reaction with Al that is originated by the  $\gamma'$ -phase, is described via  $J'$ . The latter consequently leads to a decrease in  $J_{Penetration}$  within  $d_{Trans}$ , which is indicated by the tapered shape of the arrow. Underneath  $Z_2$  no alumina particles are formed yet. Since the oxygen flux  $J_{Penetration}(Z=Z_2)$  that remains at  $Z_2$  leads to saturation of oxygen at  $Z > Z_2$ , alumina formation sets in within this most recently accessed region as soon as a critical level is reached. As the  $\gamma$ -phase preferentially enables oxygen diffusion, the entering oxygen flux at  $Z_1$  is directly correlated to the channel width  $S_\gamma$ . In other words, lower  $\gamma'$ -volume fraction results in wider matrix channels and higher oxygen flux. Thus, the remaining magnitude of  $J_{Penetration}(Z=Z_2)$  must reflect the initial oxygen flux at  $Z_1$  as a consequence of the volume fraction. Since the Al release rate of the  $\gamma'$ -phase is limited, as indicated by the delayed Al depletion at position (2) in Table 3, it is reasonable to assume that  $d_{Trans}$  is positively correlated to  $J_{Penetration}(Z=Z_2)$ . Consequently, an exaggeration of the oxygen flux due to an increased channel width must ultimately lead to a wider transition zone,  $d_{Trans}$ , in order to be counterbalanced by the lateral Al-supply. These considerations can qualitatively elucidate the dependency between  $d_{Trans}$  and the  $\gamma'$ -volume fraction shown in Fig. 9. It should be emphasized that direct proportionality between the channel width and the oxygen flux  $J_{Penetration}$  at  $Z_1$  could only be anticipated, if the presumption of constant phase-composition held, as described in chapter 2.1. However, at least the assumption of a positive correlation between channel width and resulting oxygen flux can be assumed, regarding Fig. 9. Comparing  $d_{Trans}$  for different temperatures (e.g., VF40 in Fig. 9), it is unequivocal that the thicknesses decrease with increasing exposure temperatures. Since samples for identical exposure times are compared, this tendency might be a consequence of a reduction of the oxygen flux density  $i$  at the IOF due to an increased overall oxide thickness. Additionally, a higher Al mobility in the alloy at higher temperatures could be causative, leading to an increase in  $J'$ . Both effects condition an ultimate reduction of  $J_{Penetration}$ . As this argumentation considers a less exaggerated oxygen penetration and increased Al availability, it might therefore also be capable to explain the coarsening of the alumina precipitates with increasing temperature (s. Figure 7). It should be stated that even after 500 h of exposure at 900 °C, no formation of an uninterrupted protective alumina scale took place (s. Figure 8). Instead alumina formation is observed along the  $Co_3W$  precipitates, showing an influence of not solely the  $\gamma'$ - but also the TCP-phase on the morphology of the IOF.

An interim summary (findings on polished samples):

- The alloys of high  $\gamma'$ -volume fractions provided increased oxidation resistance (reduction of mass-gain).
- For none of the polished samples that were heated in synthetic air a protective alumina scale could be observed (up to 500 h at 900 °C for VF50).

- Insufficient Al transport and exaggerated oxygen transport are supposed to cause alumina to nucleate as distinct particles that do not coarsen sufficiently to form an uninterrupted diffusion limiting alumina scale.
- Increasing  $\gamma'$ -volume fraction by rising the content of W and Ta leads to a slower propagation of the IOF in the  $\gamma$ -channels.
- High contents of W and Ta as well as long exposure times and exposure temperatures foster TCP formation. TCP-phases strongly deflect the growth of oxide phases at the internal oxidation front.

## Influence of Shot-Peening and Heating Atmosphere

### Alloy Specific Differences Regarding Defect Formation and Deformation

Before an elucidation of the effect of shot-peening on oxidation is presented, the microstructure prior to exposure is assessed. Therefore, cross-sections are provided in Fig. 11. Due to plastic deformation, the geometry and the characteristic regular alignment of the hardening-phase (as depicted in Fig. 1) is strongly affected for all alloys. In surface proximity, severe deformation is noteworthy leading to a loss of the initial precipitate morphology. For VF60 this deformation-affected zone is the least pronounced (Fig. 11d).

Deformation-induced defects (cracks and voids marked by solid-line arrows) are visible within this zone for all alloys. However, an increase of defects toward lower volume fractions clearly prevails. The vast majority of these defects is linked to the surface which is especially striking in case of VF20 (Fig. 11a), whereas the defects are isolated for VF40, VF50, and VF60, they possess a pronounced degree of interconnectivity in the case of VF20. Also, these artefacts expand deeper into alloys with smaller volume fractions. This trend is assumed to be caused by a stronger degree of deformation, due to a presumably lower yield stress of VF20 compared to the other investigated alloys. The rod-like arrangement of the cuboidal precipitates in VF20 according to Fig. 1 (no homogeneous distribution) is also notable in this context, whereas occurrence of defects as well as strongly deformed precipitates certainly declines with surface distance, the evolution of deformation bands dominates the appearance of the microstructure in deeper regions. Exemplarily, two of these features are marked by the dashed arrows in Fig. 11c, even though they can be found for all volume fractions.

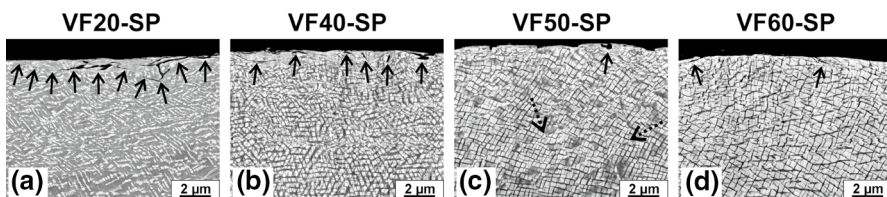


**Fig. 11** BSE-micrographs (cross-sections) of shot-peened samples. **a** VF20, **b** VF40, **c** VF50, and **d** VF60. Black arrows with solid lines mark cracks and voids in surface proximity. Dashed arrows in **c** indicate the alignment of deformation bands



Electron backscatter diffraction (EBSD) was additionally used to provide inverse pole figure (IPF) maps. The maps in Fig. 12 exhibit a qualitatively similar appearance, i.e., two deformation-affected zones can be subdivided in each case, which are exemplarily highlighted in Fig. 12d. Within zone (I) - where plastic deformation mostly prevails - the quality of the electron backscatter patterns was insufficient to allow a meaningful evaluation. Therefore, the invalid impression of apparently isotropically orientated grains in sub-micron size arises. To substantiate this interpretation, Fig. 12e depicts an electron backscatter pattern gained exemplarily for VF40 at the highlighted position in Fig. 12b. It is obvious that no or at least solely insufficient patterns were obtained within this zone. For comparison, an electron backscatter pattern of the undeformed single-crystalline area of the same sample is depicted in Fig. 12f. The thickness of zone (I) is largest for VF20 and smallest for VF60, whereas it is about the same width for VF40 and VF50. Underneath this layer, zone (II) is allocated in which local domains of other orientations than the substrate predominate (s. Figure 12d). The latter is locally interlaced by strongly deformed slices that match the orientation of the deformation bands as described for Fig. 11c. The

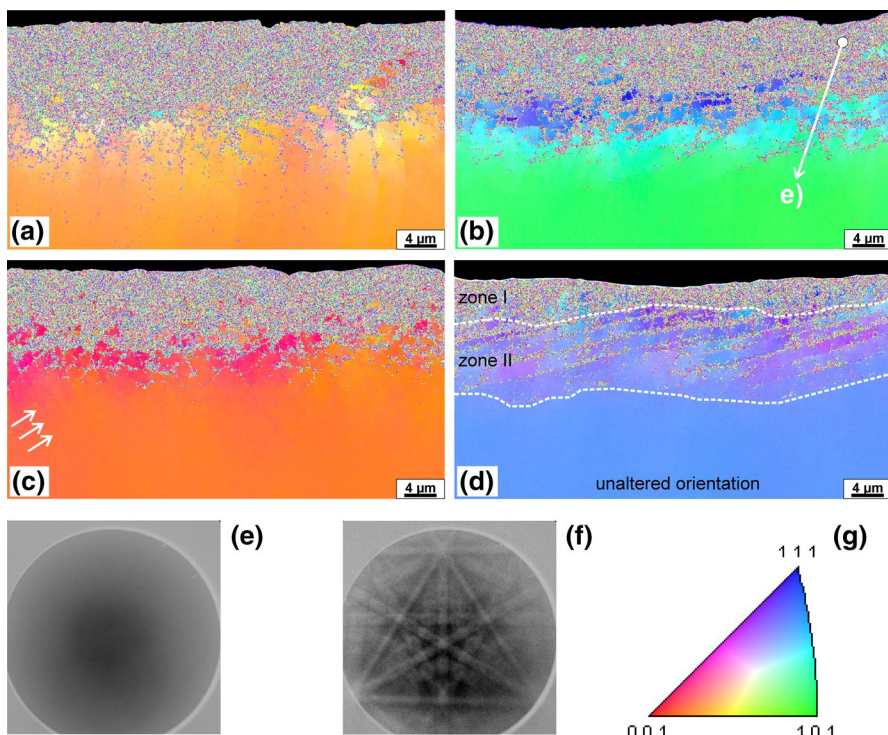


**Fig. 12** Influence of the  $\gamma'$ -volume fraction on the shot-peened induced depth of deformation. IPF maps of cross-sections of SP-alloys, with: **a** VF20, **b** VF40, **c** VF50 with highlighted deformation bands (s. text), and **d** VF60 with highlighted zones I and II (s. text). **e** electron backscatter pattern of highlighted area in **b**. **f** electron backscatter pattern of single-crystalline area of **b**. **g** Stereographic triangle for  $\gamma$ -phase

deformation bands comprise zone (I) appearance due to poor Kikuchi pattern quality in the upper part of zone (II). However, the IPF maps of VF20, VF40, and VF50 indicate a deeper penetration of the deformation bands than the occurrence of the unindexed measuring points suggest (exemplarily marked by arrows in Fig. 12c). This behavior is strikingly different to VF60, where an abrupt transition between zone (II) and the substrate occurs. A second noteworthy difference is an increasing degree of preferred orientation of the deformation bands toward increasing volume fractions.

### Elimination of Effects Derived from Surface Contamination and Roughness

To estimate the impact of surface contamination (residual indented glass-shot particles), surface roughness, and defects in surface proximity on oxidation, the extensive procedure, illustrated in Fig. 13, was conducted. Therefore, a sample of VF40 was partially shot-peened with the help of a mask, s. Figure 13a, and subsequently ground and polished (1  $\mu\text{m}$ ) prior to oxidation. By comparing Fig. 13b

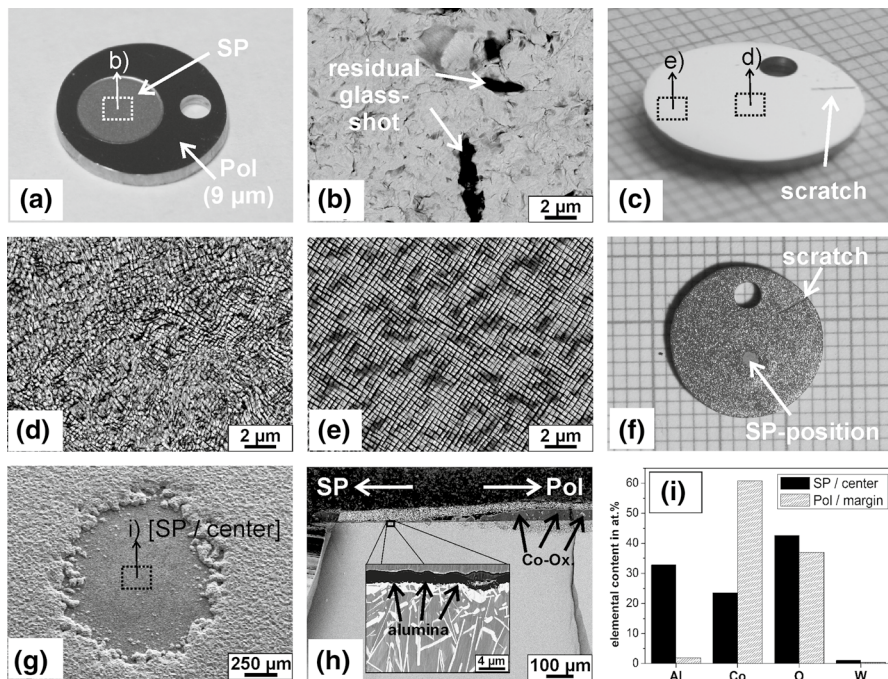


**Fig. 13** Influence of deformation on oxide growth for VF40 oxidized at 900 °C for 36 h (argon). **a** VF40 polished (9  $\mu\text{m}$ ) and partially shot-peened with the help of a mask. **b** surface of SP area after ultrasonic cleaning. **c** sample shown in a, carefully ground with 1200 grit size and subsequently polished (1  $\mu\text{m}$ ). **d** deformed microstructure in sample center. **e** sample margin, undeformed. **f** sample after exposure. **g** SE-micrograph of modified (SP + Pol) area and neighboring margin after exposure. **h** BSE-micrograph (cross-section), white arrows indicate position of sample margin (Pol) and sample center (SP). **i** SEM-EDX results of surface oxides

and c, successful removal of the mentioned surface artefacts is evident. Unlike the undeformed microstructure at the sample's margin (Fig. 13e), the appearance at the SP-affected area is dominated by strongly deformed  $\gamma'$ -precipitates that neither show cuboidal geometry nor an ordered alignment (Fig. 13d). To facilitate an easier recognition of the region of interest, the sample was marked by scratching (Fig. 13c) prior to exposure. The effect of deformation on oxidation can already be recognized by optical inspection (Fig. 13f) and becomes more striking during electron microscopic investigation of the sample surface (Fig. 13g). After exposure, the deformed part of the sample is covered by a significantly thinner oxide scale compared to the surrounding region that exhibits considerable growth of an external oxide scale. The cross-section that is displayed in Fig. 13h further elucidates this matter. Particularly, the enrichment of Al in the surface oxide grown on the deformed center of the sample (marked with "SP/center") is noteworthy. This finding is supported by the dark appearance in the BSE-micrographs (Fig. 13h), and the EDX results that are demonstrated in Fig. 13i. The introduction of cold work in a highly localized region of the surface proved that plastic deformation by itself fosters alumina scale growth and significantly suppresses the growth of Co oxides, since surface artefacts were eliminated by polishing. The EDX results of Fig. 13i correspond to the EPMA maps for as-peened samples (without masking) that were shown in Fig. 4c in comparison with polished samples in Fig. 4b.

### Implications of Surface State and Heating Conditions on Scale Growth

The diagrams in Fig. 14 reveal the impact of shot-peening and the heating atmosphere on the oxidation resistance at 900 °C during 36 h of exposure for all alloys.

For all *polished samples* only a minor impact of the heating atmosphere on the oxidation resistance was observed (Fig. 14). For VF20 (Fig. 14a), the oxidation kinetics show the highest dependency of the heating atmosphere among all polished samples, i.e., argon causing a reduction of the specific mass-gain during exposure. When comparing the TGA results that are shown in Fig. 14 with those of Fig. 2c (air, pol) it must, however, be stated that due to an insufficient reproducibility of the recorded data, besides for VF20, no clear dependency of the heating atmosphere on the oxidation behavior can be concluded in case of polished samples. Alterations of oxidation processes that are not apparent from the mass-gain curves in Fig. 14 might be revealed by elucidating the respective cross-sections. Figure 15 demonstrates electron micrographs of multilayered oxide scales after heating in argon and subsequent 36 h oxidation for all polished samples, except VF20. In the case of VF20, severe scale spallation occurred during cooling and therefore no cross-sections can be provided regardless to the heating atmosphere. A tendency of increased oxidation resistance, due to a heating step conducted in argon instead of synthetic air is indicated by the thermogravimetric data in Fig. 14a. Fast reaction kinetics (Figs. 2 and 14) indicate the formation of thick oxide scales on samples of VF20. The extensive transport of cations is presumably accompanied by the formation of pores in the inner oxide layer. In combination with thermal mismatch stresses that arise during cooling, the specimens of VF20 are particularly prone to spallation. Therefore, it was not possible to prepare cross-sections from this alloy

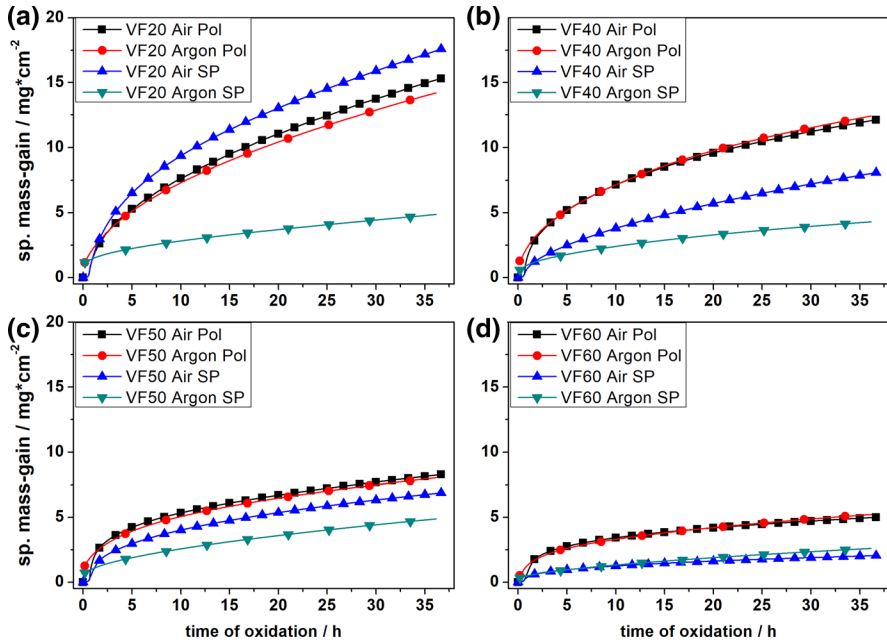


**Fig. 14** Continuous specific mass-gain (mass-gain per surface area) for polished (pol) samples and shot-peened (SP) samples oxidized for 36 h at 900 °C either heated in argon (argon) or synthetic air (air). **a** VF20, **b** VF40, **c** VF50 and **d** VF60

after exposure. Micrographs a, b, c for air- and d, e, f for argon experiments provide an overview of VF40, VF50 and VF60 (Fig. 15). It can be concluded that qualitatively the appearance of the oxide scales is not significantly influenced by the heating atmosphere. Quantitatively, however, it is worth to mention, that the outer oxide scales have higher porosity for samples that were heated in argon. This is especially pronounced for VF60, s. Figure 15f, and explains the higher outer scale thickness of VF60 argon-Pol (f) compared to VF60-Air-Pol (c) while taking the mass-gain results into account. For all polished samples needle-like precipitates ( $\text{Co}_3\text{W}$ ) can be found in the IOZ (a, b, c, d, e (case I)) or additionally as locally formed zones underneath the IOZ for VF60 argon-Pol (f (case II)).

In the following, the impact of heating atmosphere on *shot-peened samples* is elucidated. The oxidation resistance of the latter is not only generally different to their polished counterparts, shot-peening also leads to significantly increased influence of the heating atmosphere, s. Figure 14. This is especially pronounced for VF20, (a), whereas shot-peening results in a tremendous increase in the oxidation resistance when heated in argon, the oxidation resistance is severely decreased when heated in air. In agreement with the mass-gain results, Fig. 15j indicates the formation of an outer alumina scale followed by an Al depleted zone with  $\text{Co}_3\text{W}$ -formation for VF20 argon-SP. Due to the extensive mass-gain in case of VF20-Air-SP, considerable growth of protective alumina can be excluded even without having respective cross-sections on hand.

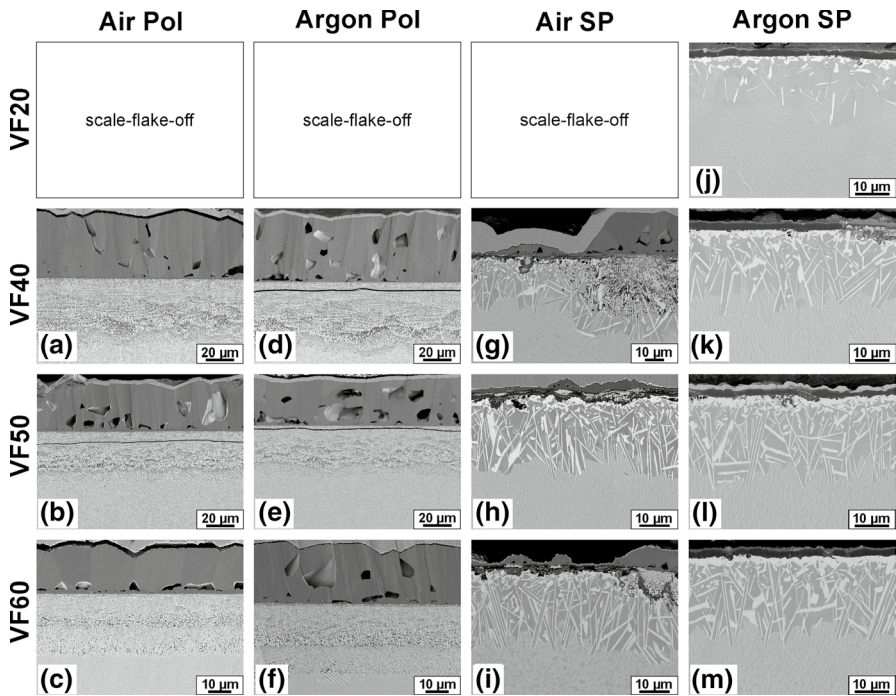


**Fig. 15** BSE-micrographs of cross-sections after 36 h exposure at 900 °C for elucidation of the influence of the heating atmosphere and surface finish. **a** (VF40), **b** (VF50) and **c** (VF60) refer to polished samples heated in air, whereas **d** (VF40), **e** (VF50) and **f** (VF60) refer to polished samples heated in argon. **g** (VF40), **h** (VF50) and **i** (VF60) refer to SP samples heated in air, whereas **j** (VF20), **k** (VF40), **l** (VF50) and **m** (VF60) refer to SP samples heated in argon. Since VF20 suffered from severe spallation during cooling that hindered the preparation of cross-sections, solely micrograph **j** is given

For VF40 and VF50 shot-peening results in mass-gain kinetics significantly below those of their polished counterparts for both heating atmospheres. This can also be confirmed by evaluating the scale appearance, s. Figure 15. For VF40 and VF50, it is remarkable that heating in argon strongly fosters continuous alumina scale formation (compare Fig. 15g and k as well as h and l, respectively). The formation of alumina was exemplarily examined by EPMA investigations for VF40 argon-SP in more detail, s. Figure 4c. The displayed maps show a pronounced oxygen and Al enrichment only within the outer oxide scale. For VF60-SP, mass-gain results on a first glance imply that heating in air could be beneficial. However, this is most certainly a consequence of the sample's thickness that was exceptionally higher for this particular sample. As solely the front- and back-sides of the samples are affected by shot-peening and not the shell surface, the pronounced oxidation kinetics of the margin might have led to this peculiarity. This is substantiated, since the cross-sections reveal that for VF60-Air-SP a quite inhomogeneous alumina scale formed, whereas it strongly increased its integrity and protectiveness by heating in argon.

As already pointed out within the introduction of this study, the degree of cold work (e.g., due to shot-peening) is one parameter affecting the mobility of a solute in an alloy. Generally, the near-surface zones of shot-peened samples possess higher solute diffusivities than the respective polished counterparts due to short-circuit diffusion paths. Two different mechanisms can be operational. Firstly, an increased dislocation density and i.e., an accelerated transport within the dislocations cores is possible (dislocation pipe diffusion) [36]. Secondly, also grain boundaries might form due to recrystallization during exposure and foster elemental transport what is described by e.g., Leistikow et al. for alloy 800 (grain boundary diffusion [30, 37]). It is pointed out by Leistikow that the mass-gain correlates in good approximation linearly with the grain size, as long as grain boundary diffusion is by orders of magnitude higher than the bulk diffusivity. At temperatures beyond 900 °C, the grain size is described as less important in the case of alloy 800, since the bulk diffusivity approaches the grain boundary diffusivity [31]. Besides the transport properties due to lattice defects, also effects derived from microstructural changes induced by plastic deformation should be considered. Figure 11, Fig. 12 and Fig. 13d depict clearly that the shot-peening induced deformation affects the geometry of the hardening-phase,  $\gamma'$ . The precipitates of shot-peened samples lost the cubic symmetry and are either distorted or partially disaggregated. Therefore, an increase in the interface/volume ratio of the disaggregated precipitates or a smaller spatial separation of both phases can be concluded. This is seen to be beneficial for protective scale formation, since localized alumina nuclei are expected to spread more homogeneously over the sample surface in order to coarsen and finally form a protective layer. In other words, the average diffusion length of Al in the alloy to enable a continuous alumina scale, is lowered by a reduction of the distance between the single Al-reservoirs. However, not solely the diffusion properties of Al might be affected. According to results from Optasanu et al. for pure Zr, mechanical stresses can also affect the oxygen penetration into the sample. A shot-peened sample is characterized by an outer zone that is prone to compressive stresses, which are compensated by a zone of tensile stresses underneath. Based on the precondition that the material expands when oxygen penetrates into its lattice, the outer zone (compressive stresses due to SP) exhibits a diffusion limiting impact, whereas the tensile zone underneath fosters the penetrating oxygen fluxes. The compressive outer zone of a SP sample of the VF alloys might therefore also be characterized by a lower oxygen mobility than a polished sample what might further explain the fostered alumina formation of shot-peened samples in this work [38]. If all these effects sufficiently prevail, a switch of the mechanism from internal to external oxidation due to protective alumina scale growth should be facilitated, regarding the Wagner criterion [11]. The decreased oxidation kinetics for VF40, VF50 and VF60 in shot-peened state compared to polished samples (Fig. 14 b, c and d), as well as the corresponding increase in alumina enriched zones according to the cross-sections (Fig. 15 g, h and i) can be directly justified. Internal oxidation and outer Co-rich oxides of still substantial thickness remained, however, locally present, indicating a pronounced transient oxidation prior to lateral alumina growth for all air experiments of SP samples. Contrary to VF40, VF50 and VF60, in the case of VF20, shot-peening—according to the TGA measurements - did obviously not sufficiently foster lateral alumina formation (VF20-Air-SP, Fig. 14 a)).

Furthermore, severe scale spallation during cooling hindered the preparation of any cross-sections (Fig. 15). Exceptionally for VF20, the applied shot-peening procedure is causative for this deteriorative effect (Fig. 14a). As described in Sect. 3.2.1, alloy specific differences regarding shot-peening induced defect formation are observed. Besides a severely deformed sample margin that can be found for all alloys, especially for VF20 pronounced formation of defects like cracks and voids (Fig. 11a) is noteworthy. Partially the size of the cracks is close to the resolution limit of the SEM. Furthermore, the defects showed a certain degree of interconnectivity. During oxidation, these artefacts are suspected to foster significant oxygen penetration into the outermost strongly deformed margin of the sample (exemplarily designated as zone (1) in Fig. 12d). According to this argumentation, a considerable amount of the deformed margin, where increased solute mobility prevails, might be excluded from the formation of an adherent alumina layer. Consequently, the exaggerated oxygen penetration in case of the air experiments cannot be compensated with an adequate countercurrent flux of Al, since the remaining deformation-affected zone is either too thin or provides a too small degree of deformation. In contrast to the air experiments, a reduced oxygen penetration together with a remaining deformation affected zone that is not prone to crack formation is believed to be causative for the successful alumina formation in case of the argon experiments.

### Combined Impact of Cold Work and Low Oxygen Partial Pressure

Heating in Argon decisively decreased the growth of external Co oxide and fostered alumina formation for all shot-peened samples but only had a minor effect on polished samples, s. Figure 14 and Fig. 15. The impact of the oxygen partial pressure on oxide formation is already addressed in the literature for various systems. Chen et al. conducted similar experiments by also comparing samples oxidized totally in air and samples of which heating was conducted in vacuum [39]. The study attributes a strong impact of the oxygen availability during heating on the duration of the transition from the initial oxidation stage to steady state oxidation for Ni-20Al-5Cr at 1100 °C [39]. When heating was conducted in vacuum ( $10^{-5}$  atm oxygen partial pressure), protective alumina formation was much faster, resulting in thinner unprotective outer oxide scales compared to samples that were heated in air [39]. It was confirmed that hampering the start of fast oxidation during heating in vacuum significantly suppresses the formation of transient oxides (e.g., NiO and  $\text{Ni}(\text{Cr},\text{Al})_2\text{O}_4$ ). TOF-SIMS investigations of a sample that was directly cooled after heating in vacuum (and not exposed to air) demonstrated increased Hf- and Y-concentrations (as well as oxygen) at the surface and in a zone of 100  $\mu\text{m}$  thickness underneath, whereas the other elements did not show as a strong deviation from the initial composition in the alloy [39]. Since the oxides of Hf and Y are thermodynamically more stable than alumina, this effect might also be involved in the argon experiments of this study, with the role of the REs transferred to Al as the element forming the most stable oxide in this system.

Duval et al. investigated the effect of oxygen partial pressure on the high-temperature oxidation of the Ni-base superalloy IN617 (24.13 at. % Cr, and 2.21 at. % Al) at 850 °C [40]. According to this work, at an oxygen partial pressure of  $10^{-5}$  atm

selective oxidation prevailed since exclusive formation of alumina, chromia and titania took place. In spite of what their formation enthalpy indicates, the growth of less stable oxides, e.g., Co oxide and Ni oxide, was not observed [40]. These results indicate that also in the case of the VF alloys, an absence of Co oxide formation might not necessarily be justifiable solely by thermodynamic reasons.

In the following, we elucidate *thermodynamic issues* for the present study. In the case of an oxygen partial pressure below the dissociation pressure of Co oxides but above the dissociation pressure of alumina, the first will not be formed during heating and exclusive alumina growth would be initiated. This interrelation is worth to be briefly discussed. The heating step was conducted in impure argon (Ar 5.0<sup>®</sup>, Linde, purity > 99.999%) containing maximum 2 ppm residual oxygen, equaling to an oxygen partial pressure of roughly  $2.96 \times 10^{-6}$  atm. The latter might be further decreased during the heating period according to in situ measurements of a recent publication by Bataillou et al. who described a considerable oxygen consumption due to the reaction of carbon-containing impurities within the furnace chamber during heating [41]. This effect was however, not elucidated in the course of this work. At the approximated oxygen partial pressure in argon,  $\text{Co}_3\text{O}_4$  is thermodynamically stable up to 600 °C, meaning that its impact on scale growth might be restricted to the first 25 min of heating [42]. Kitaoka et al. confirmed this role of the heating step on oxide formation [43]. Even though solely  $\alpha\text{-(Al,Cr)}_2\text{O}_3$  was expected to form at  $10^{-9}$  atm at 1050 °C on Co-28Ni-21Cr-16Al-0.3Y, growth of the less stable (Co,Ni)  $\text{(Al,Cr)}_2\text{O}_4$  was reported. The latter oxide phase was related to initial oxidation during the heating step [43]. Unlike  $\text{Co}_3\text{O}_4$ , CoO exhibits higher thermodynamic stability and can be expected to grow in the entire temperature regime (20–900 °C) [42]. According to these thermodynamic considerations, the strong simplifications (e.g., not considering effects of W and Ta) and according to the basis of the available data (the above mentioned dissociation pressures refer to pure oxides), thermodynamic reasons cannot be excluded but should not be considered as the only origin of the argon effect.

Additionally, *kinetic reasons* might play a crucial role since the low oxygen availability of the impure argon atmosphere might affect the competitive oxide growth on the surface. For both surface states, the growth of Co oxide is likely hampered during heating in argon, since the availability of oxygen (adsorbed on the surface) is the rate limiting factor [44]. The characteristic rapid growth of (typically defect-rich) Co oxides is restricted. Due to the low mobility of Al and the restricted reservoir in the alloy in the case of polished samples, lateral growth of alumina is expected to be too slow to achieve the development of a protective layer during the duration of argon exposure. Therefore, still Co oxide remains preferentially growing when the exposure atmosphere is switched to air for the oxidation step. In the case of shot-peened samples, argon leads - as for polished samples - to reduced oxidation kinetics of Co oxide. However, alumina can spread faster on the surface, since the deformed alloy sufficiently provides Al. Therefore, alumina is formed exclusively. Consequently, the subsequent growth of Co oxides remains effectively hindered.

According to the BSE-micrographs, almost no outer Co oxide is present for SP-argon samples what strongly supports this mechanism. The fact that heating in low oxygen-containing atmosphere (argon) did effectively foster alumina scale growth



also for VF20-SP, whereas poor oxidation resistance prevailed for air experiments, affirms the contemplated postulation of a defect-promoted oxygen access into the material.

Even though the entire sequence of elementary processes during heating in Ar could not be revealed, a strong correlation between the positive effect of reduced oxygen partial pressure and the sample preparation prior to exposure was demonstrated. The results indicate that a restriction of the fast growth of Co oxides by a reduction of the oxygen availability is beneficial for alumina formation only if a sufficient Al flux is obtainable.

## Conclusions

The high-temperature oxidation behavior of 4 quaternary (Co-Al-W-Ta system) Co-base model alloys with  $\gamma/\gamma'$ -microstructure was systematically investigated via isothermal thermogravimetric analysis (TGA) at 800 °C, 850 °C, and 900 °C in synthetic air for exposure times up to 36 h.

The two-phase alloys possessed differing amounts of  $\gamma'$ -phase with nominal volume fractions of 20%, 40%, 50%, and 60%, that were achieved by compositional variations (W- and Ta-content). Firstly, the impact of the  $\gamma'$ -volume fraction on oxidation was assessed for polished samples. Secondly, the role of surface deformation via shot-peening prior to oxidation was elucidated. Thirdly, the role of a reduced oxygen partial pressure during heating was addressed (whereas the subsequent isothermal oxidation at target temperature was conducted in synthetic air). According to TGA results and subsequent microscopic investigations of the oxide scales the following conclusions can be drawn:

- The alloys of high  $\gamma'$ -volume fractions provided increased oxidation resistance (reduction of mass-gain).
- For none of the polished alloys a protective alumina scale could be observed. Instead, outer Co-rich scales of substantial thickness were formed, followed by pronounced internal oxide scales underneath.
- Insufficient Al transport and exaggerated oxygen transport are supposed to cause alumina to nucleate as discrete particles that do not coarsen sufficiently to form an uninterrupted diffusion limiting alumina scale in the case of polished samples.
- Increasing  $\gamma'$ -VF by rising the content of W and Ta leads to a slower propagation of the IOF in the  $\gamma$ -channels.
- High contents of W and Ta as well as long exposure times and exposure temperatures foster TCP formation. TCP-phases strongly deflect the growth of oxide-phases at the internal oxidation front.
- The mobility of Al in subsurface-regions increases with the density of defects that were implemented via shot-peening. If a sufficient Al flux is obtainable, the reduction of the oxygen availability during heating fosters protective alumina formation and consequently restricts the fast growth of Co oxides.

**Acknowledgements** Scientific and financial support by the Deutsche Forschungsgemeinschaft (DFG) through the Collaborative Research Center SFB-TR 103 (Project A5 and A7) is highly acknowledged. The authors would like to express their gratitude to Gerald Schmidt and Mathias Galetz as well as Nicklas Volz and Reno Ehm for conducting the EPMA measurements and the helpful discussions.

**Funding** Open Access funding enabled and organized by Projekt DEAL.

**Open Access** This article is licensed under a Creative Commons Attribution 4.0 International License, which permits use, sharing, adaptation, distribution and reproduction in any medium or format, as long as you give appropriate credit to the original author(s) and the source, provide a link to the Creative Commons licence, and indicate if changes were made. The images or other third party material in this article are included in the article's Creative Commons licence, unless indicated otherwise in a credit line to the material. If material is not included in the article's Creative Commons licence and your intended use is not permitted by statutory regulation or exceeds the permitted use, you will need to obtain permission directly from the copyright holder. To view a copy of this licence, visit <http://creativecommons.org/licenses/by/4.0/>.

## References

1. J. Sato, T. Omori, K. Oikawa, I. Ohnuma, R. Kainuma and K. Ishida, *Science* **312**, 90–91 (2006)
2. C. H. Zenk, I. Povstugar, R. Li, et al. *Acta Materialia* **135**, 244–251 (2017)
3. H. Y. Yan, V.A. Vorontsov, D. Dye, *Corrosion Science* **83**, 382–395 (2014)
4. A. M. Y. Razak, 11-Gas turbine performance modelling, analysis and optimization. in *Modern Gas Turbine Systems*, ed. P. Jansohn (Elsevier Science, Stanford, 2013), pp. 423–514.
5. S. Neumeier, H. U. Rehman, J. Neuner, et al., *Acta Materialia* **106**, 304–312 (2016).
6. B. A. Pint, J. R. Di Stefano and I. G. Wright, *Materials Science and Engineering* **415**, 255–263 (2006).
7. S. Neumeier, L. P. Freund and M. Göken, *Acta Materialia* **109**, 104–107 (2015).
8. L. Freund, S. Gies, D. Schwimmer, et al., *Journal of Materials Research* **32**, 4475–4482 (2017).
9. T. Pollock, J. Dibbern, M. Tsunekane, J. Zhu and A. Suzuki, *The Journal of The Minerals, Metals & Materials Society* **62**, 58–63 (2010).
10. C. Stewart, R. Rhein, A. Suzuki, T. Pollock, C. Levi, Oxide scale formation in novel  $\gamma/\gamma'$  Cobalt-based alloys. in *Proceedings of the 13th International Symposium on Superalloys* (2016), pp 991–999.
11. C. Wagner, *Zeitschrift für Elektrochemie, Berichte der Bunsengesellschaft für Physikalische Chemie* **63**, 772–782 (1959).
12. T. Omori, K. Oikawa, J. Sato, et al., *Intermetallics* **32**, 274–283 (2013).
13. S. Kobayashi, Y. Tsukamoto, T. Takasugi, et al., *Intermetallics* **17**, 1085–1089 (2009).
14. A. Bauer, S. Neumeier, F. Pyczak, R. Singer and M. Göken, *Materials Science and Engineering A* **550**, 333–341 (2012).
15. B. Gao, L. Wang, Y. Liu, X. Song, S. Yang and A. Chiba, *Corrosion Science* **157**, 109–115 (2019).
16. B. Nithin, A. Samanta, S. K. Makineni, et al., *Journal of Materials Science* **52**, 11036–11047 (2017).
17. C. A. Stewart, S. P. Murray, A. Suzuki, T. M. Pollock and C. G. Levi, *Materials & Design* **189**, 108445 (2020).
18. S. Kobayashi, T. Yuki and T. Takayuki, *Intermetallics* **19**, 1908–1912 (2011).
19. S. Kobayashi, T. Yuki and T. Takayuki, *Intermetallics* **31**, 94–98 (2012).
20. N. Volz, C. H. Zenk, R. Cherukuri, et al., *Metallurgical and Materials Transactions A* **49**, 4099–4109 (2018).
21. M. Weiser, M. C. Galetz, H.-E. Zschau, et al., *Corrosion Science* **156**, 84–95 (2019).
22. A. Yeh, S. Wang, C. Cheng, Y. Chang and S. Chang, *Oxidation of Metals* **86**, 99–112 (2016).
23. M. Weiser and S. Virtanen, *Oxidation of Metals* **92**, 541–560 (2019).
24. M. Weiser, R. J. Chater, B. A. Shollock and S. Virtanen, *NPI Materials Degradation* **3**, 33 (2019).

25. G. H. Meier, F. S. Pettit and A. S. Khan, High temperature oxidation of rapidly solidified Ni-Al-Mo-W Alloys, 348–359. in *Rapid Solidification Processing, Principles and Technologies*, III, ed. Robert Mehrabian, (National Bureau of Standards, Gaithersburg, MD., 1982).
26. S. Espevik, R. A. Rapp, P. L. Daniel and J. P. Hirth, *Oxidation of Metals* **14**, 85–108 (1980).
27. S. Espevik, R. A. Rapp, P. L. Daniel and J. P. Hirth, *Oxidation of Metals* **20**, 37–65 (1983).
28. D. Kubacka, Y. M. Eggeler, N. Volz, S. Neumeier, E. Spiecker, Using rapid thermal annealing for studying early stages of high-temperature oxidation of superalloys. in *Superalloys 2020*, Tin S. et al., eds.; The Minerals, Metals & Materials Series, (Springer, Cham, 2020) pp 763–770.
29. M. Weiser, Y. M. Eggeler, E. Spiecker and S. Virtanen, *Corrosion Science* **135**, 78–86 (2018).
30. H. J. Grabke, E. M. Müller-Lorenz, S. Strauss, E. Pippel and J. Woltersdorf, *Oxidation of Metals* **50**, 241–254 (1998).
31. S. Leistikow, I. Wolf and H. J. Grabke, *Werkstoffe und Korrosion* **38**, 556–562 (1987).
32. F. Wang, *Oxidation of Metals* **48**, 215–224 (1997).
33. A. Bezold, N. Volz, F. Xue, C. H. Zenk, S. Neumeier and M. Göken, *Metallurgical and Materials Transactions A* **51**, 1567–1574 (2020).
34. L. Klein, A. Bauer, S. Neumeier, M. Göken and S. Virtanen, *Corrosion Science* **53**, 2027–2034 (2011).
35. W. Zhao, Y. Kang, J. Orozco and B. Gleeson, *Oxidation of Metals* **83**, 187–201 (2015).
36. R. Smoluchowski, *Physical Review* **87**, 482–487 (1952).
37. J. C. Fisher, *Journal of Applied Physics* **22**, 74–77 (1951).
38. V. Optasanu, A. Kanjer and T. Montesin, *Annales de Chimie Science des Matériaux* **40**, 69–77 (2016).
39. W.-T. Chen, B. Gleeson and A. Heuer, *Oxidation of Metals* **92**, 137–150 (2019).
40. A. Duval, F. Miserque, M. Tabarant, et al., *Oxidation of Metals* **74**, 215–238 (2010).
41. L. Bataillou, L. Martinelli, C. Desgranges, et al., *Oxidation of Metals* **93**, 329–353 (2020).
42. I. Barin, *Thermochemical data of pure substances—Part 01*, (Wiley, New Jersey, 2008).
43. S. Kitaoka, T. Kuroyama, M. Matsumoto, R. Kitazawa and Y. Kagawa, *Corrosion Science* **52**, 429–434 (2010).
44. S. Mrowec and K. Przybylski, *Oxidation of Metals* **11**, 365–381 (1977).

**Publisher's Note** Springer Nature remains neutral with regard to jurisdictional claims in published maps and institutional affiliations.

## Authors and Affiliations

S. P. Hagen<sup>1</sup>  · M. Weiser<sup>1</sup> · D. Kubacka<sup>2</sup> · E. Spiecker<sup>2</sup> · S. Virtanen<sup>1</sup>

M. Weiser  
martin.weiser@fau.de

D. Kubacka  
dorota.kubacka@fau.de

E. Spiecker  
erdmann.spiecker@fau.de

S. Virtanen  
virtanen@ww.uni-erlangen.de

<sup>1</sup> Chair for Surface Science and Corrosion, Friedrich-Alexander Universität Erlangen-Nürnberg, 91058 Erlangen, Germany

<sup>2</sup> Institute of Micro- and Nanostructure Research (IMN) and Center for Nanoanalysis and Electron Microscopy (CENEM), Friedrich-Alexander Universität Erlangen-Nürnberg, 91058 Erlangen, Germany